Biophysical Journal, Volume 97

Supporting Material

Multi-scale analysis of dynamics and interactions of heterochromatin protein 1 by fluorescence fluctuation microscopy

Katharina P. Müller, Fabian Erdel, Maïwen Caudron-Herger, Caroline Marth, Barna D. Fodor, Mario Richter, Manuela Scaranaro, Joël Beaudouin, Malte Wachsmuth, and Karsten Rippe

Supplementary Methods

Plasmids

Suv39h1 and HP1β cDNA fragments were derived by PCR from plasmids pGeX2T-Suv39h1 and pET-16b-HP1β, kindly provided by Ken Yamamoto (Kyushu University, Japan) and Natasha Murzina (University of Cambridge, UK). These were cloned into the vectors pEGFP-C1 (BD Biosciences Clontech, Heidelberg, Germany) or pTagRFP-C (Evrogen, Moscow, Russia), respectively, to generate expression vectors for the autofluorescent fusion proteins GFP-Suv39h1, TagRFP-Suv39h1, GFP-HP1β and TagRFP-HP1β. Labeling of chromatin was accomplished via mRFP1-labeled histone H2A by transient transfection (1).

Cell lines

The stable GFP-HP1α cell line clone was isolated in a screen to identify mouse pericentric chromatin proteins. A retrovirus-based gene trap vector (pRet_1L-Neo, unpublished data) was used to infect NIH 3T3 cells. The vector carried a mouse PGK promoter-driven FLAG-HA-GFP cassette without a stop codon, followed by a splice donor site. The infected cells were screened for focal GFP enrichment, and the fusion partner was determined by 3'-race with GFP-specific primers. The sequence information obtained from the GFP-HP1α clone indicates that the GFP cassette is spliced to exon 7 of endogenous HP1α transcripts. In the predicted fusion protein product (FLAG-HA-eGFP-full-length-HP1α) an additional NLVAILLQVDQQAHD amino acid sequence (translation of the noncoding 5' region of exon 7) separates the two moieties. This cell line is referred to here as 3T3-HP1α. To investigate the contribution of the Suv39h1/h2 methylases on HP1 binding immortalized mouse embryonic fibroblast (iMEF) cells were used (2). In these experiments wild type (iMEF-wt) and double null mutant (iMEF-dn) cells were compared, in which the Suv39h1 and Suv39h2 gene loci were disrupted. Accordingly, the iMEF-dn cells lack H3K9 di- and trimethylation in pericentric heterochromatin.

Cell culture

NIH 3T3 mouse fibroblasts, the 3T3-HP1α cell line as well as the iMEF-wt and the iMEF-dn cell lines were cultured in tissue culture flasks at 37 °C in a water-saturated 5 % CO_2 atmosphere, using Dulbecco modified eagle medium (DMEM) without phenol red, supplemented with 10 % fetal calf serum, 2 mM L-glutamine, penicillin/streptomycin (each at 100 µg/ml) and 0.35 g/ml glucose. For live imaging experiments cells were cultured to 60 – 80 % confluency on chambered microscopy slides (Nunc, Wiesbaden, Germany) as previously described and were kept in Leibovitz's L15-medium (Invitrogen, Karlsruhe, Germany) supplemented with 10 % fetal calf serum and pen/strep during live experiments. The measurements were carried out at room temperature. Transient transfection was performed with Effectene (Qiagen, Hilden, Germany) for NIH 3T3 cells and TurboFect (Fermentas, St. Leon-Roth, Germany) for iMEFs according to the protocol of the manufacturer. For imaging of fixed samples, the cells were incubated for 1 - 2 days after transfection and then fixed in 4 % paraformaldehyde (PFA) for 7 minutes at room temperature. Immunostaining of fixed cells was conducted with a primary anti-H3K9me3 antibody (Abcam, Cambridge, UK) and subsequent visualization with a secondary goat anti-rabbit Alexa 568 antibody (Invitrogen, Molecular Probes). Chromatin staining was accomplished with 5 µg/ml Hoechst 33342 or 0.5 µg/ml DAPI (Invitrogen, Molecular

Probes). All coverslips were mounted using Mowiol (10 % Mowiol 4-88, 25 % glycerol in 100 mM Tris·HCl pH 8.5).

Western blot

NIH 3T3 cells stably expressing GFP-HP1α were harvested by trypsination and lysed in ice-cooled buffer containing 10 mM Tris·HCl pH 7.5, 150 mM NaCl, 0.5 mM EDTA, 0.1 % NP40, 1 mM PMSF, and a protease inhibitor cocktail (Roche, Mannheim, Germany). After SDS-PAGE the proteins were transferred to a nitrocellulose membrane (Whatman GmbH, Dassel, Germany) and incubated with the primary antibody anti-HP1α (1:1000 dilution, C7F11, Cell Signaling, Danvers, MA, USA) overnight at 4 °C, washed three times with TBS/0.1 % Tween and incubated with a secondary HRP-conjugated antibody (anti-rabbit, 1:2000 dilution, Cell Signaling, Danvers, MA, USA) for 1 hour and washed 3 times with TBS/0.1 % Tween. Bound antibodies were detected using a chemiluminescent ECL reagent (1 ml 0.1 M Tris·HCl pH 7.5 supplemented with 0.25 mg Luminol, 0.3 µl H_2O_2, 100 µl DMSO, 0.11 mg para-hydroxycumarine acid) and an imaging film. For quantification, DyLight 800-conjugated secondary antibodies (anti-rabbit, Pierce Biotechnology, Rockford, IL, USA) were used and the signal was recorded with a LI-COR Odyssey infrared detection system (LI-COR Biosciences, Bad Homburg, Germany).

Fluorescence microscopy setup

For confocal imaging, FRAP and FLIP a Leica TCS SP5 confocal laser scanning microscope (CLSM) equipped with a HCX PL APO lambda blue 63x/1.4 NA oil immersion objective lens was used (Leica Microsystems CMS GmbH, Mannheim, Germany). A diode-pumped solid state laser and an Argon ion laser were used for DAPI ($\lambda = 405$ nm), GFP ($\lambda = 488$ nm) and TagRFP ($\lambda = 514$ nm) excitation. For the multi-color analysis sequential image acquisition was applied and emission detection ranges were adjusted to minimize crosstalk between the different signals. Protein distribution and chromatin density in heterochromatin respective to euchromatin were compared by evaluating multiple spots within a cell and calculating the mean intensity values therein.
FCS and CP measurements were performed on a Leica TCS SP2 AOBS FCS2 CLSM equipped with single photon counting modules for single molecule detection (SPC-AQR-14, Perkin Elmer Optoelectronics, Fremont, CA, USA). For intracellular measurements a HCX UPlanApo 63x/1.2 NA water immersion objective lens with correction collar was used. The excitation of GFP and Alexa Fluor 488 was done with the 488 nm Argon laser line. The detection pinhole had a diameter corresponding to one Airy disk and emission was recorded through a 500 - 550 nm filter. For FCS and CP measurements the scanning mirrors were fixed at a desired recording position and the fluorescence signal was acquired with the software Vista 3.6.22 LE (ISS Inc., Champaign, IL, USA).

Fluorescence photobleaching experiments

For the FRAP experiments 50 prebleach images were taken. Laser intensities were adjusted such that the power in the sample did not exceed 10 µW, resulting in an energy deposition of less than 1 µJ per image for the selected scan speed (1400 Hz) and image size (128 x 128 pixels). The region of interest (ROI) was subjected to two high intensity laser pulses of 112 ms duration each corresponding to about two times an energy deposition of not more than 100 µJ. Postbleach images were collected at 112 ms time intervals for 60-100 s with the

laser intensity attenuated to the same as in the prebleach images. To characterize the slow mobility fraction in heterochromatin the data acquisition was extended to ~ 300 s. For the FRAP profile analysis a bar of 3 µm in height crossing the whole cell nucleus was photobleached, while the intensity-based analysis was conducted for a circular ROI of effective 1.9 µm in diameter. The illumination of the cells with relatively high laser intensity during the bleaching process could potentially compromise the integrity of the GFP tagged protein and change its mobility and interaction properties. Under the conditions used here the illumination during bleaching appears to have no significant effect since the analysis of HP1α mobility by methods with very different energy deposition (FRAP, CP and FCS, see below) gave consistent results. This is consistent with the previously reported findings that local heating during photobleaching does not exceed 0.5 K under the conditions used here and has no significant effect on macromolecular mobility (3-5). Furthermore, it was confirmed that multiple FRAP experiments in the same cell gave identical results within the error of the measurements. The cell viability was not affected, which is attributed to the fact that for fluorescent proteins the generation of free radicals is largely reduced as compared to synthetic dyes (6).

Profile FRAP analysis (pFRAP)

An analysis of the bleach profile shape during the fluorescence recovery time course was conducted (7). The fluorescence intensity was averaged in parallel to the bleach strip to calculate the intensity profile perpendicular to the strip for each picture of the time series. The profiles were normalized to the averaged prebleach values and analyzed in terms of the profile broadening. For one-dimensional strip-bleaching the postbleach distribution as initial condition is given by

$$c(y_0,0) = 1 - p\big(\Theta(y_0 - a) - \Theta(y_0 + a)\big) \qquad (1)$$

with Θ being the unit step function, a the half band width and p corresponding to the bleach depth ($p = 0$ for non-bleached regions and $p = 1$ for a completely bleached ROI). The distribution for successive time-steps can then be calculated with Eq. 2:

$$c(y,t) = 1 - \frac{p}{2}\left[erf\left(\frac{a-y}{\sigma(t)}\right) + erf\left(\frac{a+y}{\sigma(t)}\right)\right] \qquad (2)$$

by applying the transition probability (Greens function) with the boundary condition of $\sigma = 0$ at $t = 0$. Since the dimensions of the bleached strip were of similar dimensions as the cell nucleus a confined diffusion model was applied. The value of $\sigma^2(t)$, corresponding to the mean squared displacement, was calculated according to $\sigma^2(t) = r_c^2\left(1 - \exp\left(-4Dt/r_c^2\right)\right)$ with D being the diffusion coefficient and r_c the typical length scale of the accessible region. The profiles of the first 50 postbleach images (according to 5.6 s) were plotted and the data were fitted to Eq. 2 using Microcal Origin 6.0 (OriginLab, Northampton, MA, USA).

Intensity based FRAP experiments

Before fitting the data the FRAP recovery curves were corrected for acquisition photobleaching and detector noise. Image areas representing the cell and the background were selected, and the average intensity in both areas was calculated over time. For the

analysis the bleached circular region of interest (ROI) was selected and the normalized recovery curve – averaged over the selected ROI – was calculated according to the formula

$$frap(t) = \left(\frac{I_{\mathrm{ROI}}(t) - I_{\mathrm{BG}}(t)}{I_{\mathrm{Cell}}(t) - I_{\mathrm{BG}}(t)}\right)\left(\frac{I_{\mathrm{Cell}}(0) - I_{\mathrm{BG}}(0)}{I_{\mathrm{ROI}}(0) - I_{\mathrm{BG}}(0)}\right) \qquad (3)$$

with the average ROI intensity $I_{\mathrm{ROI}}(t)$, the average background intensity $I_{\mathrm{BG}}(t)$ and the average cell intensity $I_{\mathrm{Cell}}(t)$.

The time evolution of the intensity integrated over the bleach spot was analyzed according to the theoretical framework developed by McNally and coworkers (8). The size of the bleach spot (ROI) was approximated by a circle with an effective radius that accounts for the broadened initial bleach profile (9). It was determined from the intensity profile through the bleach spot measured for a fixed sample. From this a diameter of 1.5 µm corresponding to the microscope setting was measured at the bottom of the intensity profile, while the effective diameter at 50 % intensity was ~1.9 µm. The latter value was used for the quantitative analysis, in which the data were fitted either to a diffusion model, a binding model or a reaction-diffusion model that incorporates both diffusion and binding processes.

The recovery of the fluorescence intensity integrated over the bleach spot was analyzed according to the following approach: The FRAP recovery curve for the whole ROI equals the sum of the contributions from free f or bound c labeled protein $frap(t) = \bar{f}(t) + \bar{c}(t)$, with the horizontal bar indicating averages over the bleached ROI. In order to obtain a numerical solution a Laplace transform is performed and a solution for $\overline{frap}(p)$ is derived, which must be transformed back to give $frap(t)$. The parameter p denotes the complex Laplace variable (8).

$$\overline{frap}(p) = \frac{1}{p} - \frac{F_{\mathrm{eq}}}{p}\left(1 - 2K_1(q\omega)I_1(q\omega)\right)\left(1 + \frac{k^*_{\mathrm{on}}}{p + k_{\mathrm{off}}}\right) - \frac{C_{\mathrm{eq}}}{p + k_{\mathrm{off}}} \qquad (4)$$

The parameters k_{on} and k_{off} and $[S]_{\mathrm{eq}}$ denote the association rate and the dissociation rate, and the relation $k^*_{\mathrm{on}} = k_{\mathrm{on}} \cdot [S]_{\mathrm{eq}}$ defines a pseudo-association rate k^*_{on} for the case of a constant equilibrium substrate concentration $[S]_{\mathrm{eq}}$. These are related to steady-state concentrations of free and bound protein f_{eq} and c_{eq}, respectively, by

$$f_{\mathrm{eq}} = \frac{k_{\mathrm{off}}}{k^*_{\mathrm{on}} + k_{\mathrm{off}}}$$
$$c_{\mathrm{eq}} = \frac{k^*_{\mathrm{on}}}{k^*_{\mathrm{on}} + k_{\mathrm{off}}} \qquad (5)$$

I_1 and K_1 are modified Bessel functions of the first and second kind; ω is the radius of the bleach spot and q^2 is defined as

$$q^2 = \left(\frac{p}{D}\right)\left(1 + \frac{k^*_{\mathrm{on}}}{p + k_{\mathrm{off}}}\right) \qquad (6)$$

The numerical inverse Laplace transformation yields $frap$(t) that can be fitted to the recovery curve in order to obtain values for the fit parameters k^*_{on}, k_{off} and the diffusion coefficient D. Based on the ratio of the rate constants derived from quantitative FRAP analysis, a pseudo-binding constant K^*_{eq} can be calculated according to Eq. 7:

$$K_{\mathrm{eq}}^{*} = \frac{k_{\mathrm{on}}^{*}}{k_{\mathrm{off}}} = \frac{k_{\mathrm{on}}^{*}[S]_{\mathrm{eq}}}{k_{\mathrm{off}}} \qquad (7)$$

Using the definition of the pseudo-binding constant, an apparent diffusion coefficient D_{app} is defined as

$$D_{\mathrm{app}} = \frac{D}{1 + K_{\mathrm{eq}}^{*}} \qquad (8)$$

This is the relevant quantity for the description of effective diffusion processes with $k_{\mathrm{on}}^{*}\tau_{\mathrm{D}} >> 1$, and a characteristic diffusion time $\tau_{\mathrm{D}} = \omega^{2}/D$ (8). In the case of multiple binding sites, Eq. 8 has to be modified to

$$D_{app} = \frac{D}{1 + \sum_{i} \theta_{\mathrm{i}} \cdot K_{\mathrm{eq,i}}^{*}} \qquad (9)$$

with the parameters θ_i representing the relative fractions of the different binding sites. The simpler diffusion-dominant and reaction-dominant models can be derived from the reaction-diffusion model (Eqs. 4-6), for which the appropriate simplifications and the inverse Laplace transform can be calculated analytically. For the diffusion-dominant case, the solution is

$$frap(t) = e^{-\frac{\tau_{\mathrm{D}}}{2t}}\left[I_0\left(\frac{\tau_{\mathrm{D}}}{2t}\right) + I_1\left(\frac{\tau_{\mathrm{D}}}{2t}\right)\right] \qquad (10)$$

and for the reaction-dominant case, the solution it is given by

$$frap(t) = 1 - C_{\mathrm{eq}}\, e^{-k_{\mathrm{off}} t} \qquad (11)$$

At least 10 experiments each for HP1α and for HP1β were evaluated for a specific type of bleaching experiment.

Implementation of software for the analysis of FRAP recovery curves according to different models

Reaction diffusion analysis. For the half-automated FRAP analysis a software tool was implemented that is termed **F**RAP **RE**action **DI**ffusion **S**olver (*FREDIS*). *FREDIS* directly reads Leica Image Files (LIF) together with its metadata (such as the scanning speed, the acquisition time and the voxel size) that are generated by the Leica Application Suite software installed with the Leica TCS SP5 microscopes. The FRAP curve can be calculated and fitted to the models described by Eqs. 4, 10 and 11 for the determination of reaction-diffusion parameters according to the approach described previously (8). The reaction model assumes binding that is much slower than diffusion so that the latter can be neglected. The pure diffusion model describes freely diffusing proteins or transient binding with very fast exchange that is indistinguishable from a diffusive process. In contrast the reaction-diffusion model incorporates diffusion and binding effects on arbitrary time-scales. The fitting algorithm is based on a simple iterative grid search that minimizes the residuals

$$\chi^2 = \sum_i \frac{(frap_i - model_i)^2}{model_i} \qquad (12)$$

In Eq. 12 $frap_i$ represents the measured recovery at time-point i, $model_i$ represents the calculated recovery at time-point i (the sum runs over all post-bleach time-points). The calculated recovery curve is fixed at the two points indicated by the red dots in the plot below: At time 0 after the bleach it was set to 0, since control experiments with fixed cells showed that the intensity was 0 after the bleach in all planes. At the time-point of the last acquired image it was set to the average ROI intensity of the last five images. In the case of incomplete recovery the size of the immobile fraction was estimated by calculating the value of the recovery curve at infinite time, and subtracting this value from the pre-bleach intensity (i.e. the average ROI intensity of the last five pre-bleach images).

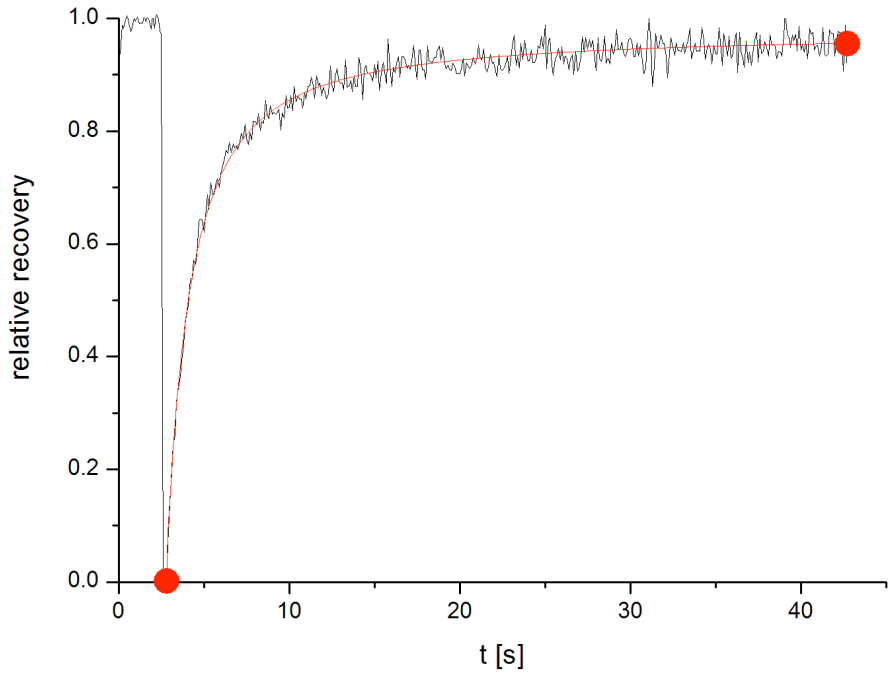

For the pure reaction and the pure diffusion model, the fitting procedure takes less than one second on a standard computer system. Thus, there is no demand for a faster second-order algorithm, and the robust grid search technique with an automatically generated initial guess can be used. However, the calculation of the recovery time course according to the reaction-diffusion model is computed numerically, and – due to the relatively slow numerical inversion of the Laplace transform – computation time is an issue. Since second-order algorithms for the reaction-diffusion model involve four inverse numerical Laplace transforms in each cycle (to calculate the gradient in three-dimensional parameter space), they are slower than the simple grid search algorithm: In comparison to the second-order Levenberg-Marquardt algorithm, the grid search algorithm converged with more cycles but needed less computational time for a typical fit. Therefore the grid search algorithm was implemented as the standard fitting procedure for all the three models.

Confidence intervals. The error limits in *FREDIS* are calculated for each fit parameter as 95 % confidence intervals. The limits of each interval are determined according to the log-likelihood criterion (10)

$$n\left[\log(\chi^2(\theta_0)) - \log(\chi^2(\theta))\right] \le \chi_p^2(\alpha) \qquad (13)$$

$\chi^2(\theta)$ represents the sum of residuals for a given parameter vector θ, θ_0 is the parameter vector in the minimum, n is the number of data points (i.e. post-bleach time points), $\chi_p^2(\alpha)$ is the upper α percentage point for the χ^2 distribution and p is the number of fit parameters. Starting at the minimum, the fit parameters are varied in both directions according to a grid search algorithm until the condition given in Eq. 13 does not hold anymore. For the pure reaction and pure diffusion models, only one parameter has to be varied and the calculation is straightforward. However, for the reaction-diffusion model three parameters have to be varied and the shape of the confidence region has to be incorporated into the calculation. This is due to the fact that an increase in the residuals caused by the change of one fit parameter can be compensated by the change of another fit parameter. In order to obtain the correct confidence interval the parameters cannot be regarded as independent. The shape of the confidence region can be estimated considering the formulas for the reaction-diffusion model and its limiting cases, the effective diffusion model and the reaction model. For moderate pseudo-association rates and small or moderate dissociation rates (compared to the characteristic diffusion times), all of the three fit parameters influence the recovery significantly. In this case, the three parameters can be regarded as independent and the confidence region resembles a sphere. For large pseudo-association rates, the dynamic behavior can be described adequately by an effective diffusion coefficient that depends only on the ratio of pseudo-association and dissociation rate (8). This results in an increasingly deformed confidence region that resembles an ellipsoid. The two-dimensional projections of this ellipsoid is depicted below in the schematic representation of confidence regions and intervals for the reaction-diffusion model at the transition to the effective diffusion regime (panel A, B) and to the pure reaction regime (panel C, D).

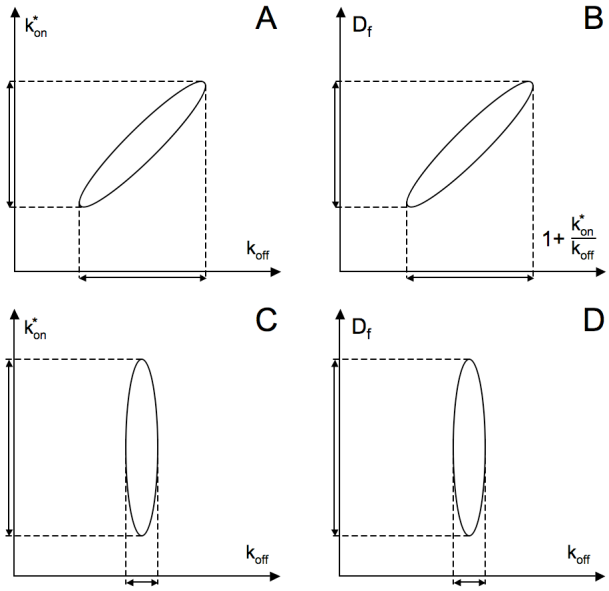

In the $k^*_{on} - k_{off}$ plane, i.e. at a fixed diffusion coefficient D, the projection of the confidence region is an ellipse: The effective diffusion coefficient depends only on the ratio of the rates that is constant on the semi-major axis of the ellipse. In the $D - k^*_{on}$ plane, the situation is similar: Since the effective diffusion coefficient can be kept constant by increasing (or

decreasing) both D and k_{on}^{*}, the projection of the confidence region is elongated and resembles an ellipse (for sufficiently large k_{on}^{*}). In analogy, in the $D - k_{off}$ plane the effective diffusion coefficient can be kept constant by increasing D and decreasing k_{off} or vice versa, resulting in an elongated projection of the confidence region as well. For small pseudo-association rates (compared to the characteristic diffusion times), the pure reaction model can describe the dynamic behavior well: In this case, the recovery depends only on the dissociation rate, resulting in growing confidence intervals for both diffusion coefficient and pseudo-association rate. The shape of the confidence region is an ellipsoid with its semi-minor axis determining the confidence interval for the dissociation rate; the two-dimensional projections are ellipses with its semi-minor axis parallel to the axis of k_{off} (see figure above). The case of diffusion is similar to the case of reaction: Instead of the dissociation rate the diffusion coefficient becomes the only important and well-defined parameter. Thus, the shape of the confidence region can be regarded as an ellipsoid that, in the case of effective diffusion, is not aligned to the axes spanning the parameter space. In this case, the confidence intervals calculated independently for the different fit parameters are too small. *FREDIS* calculates the independent 95 % confidence intervals for each parameter in the first step. Subsequently, the confidence intervals for k_{on}^{*} and k_{off} are calculated while both parameters are changed in a way that the effective diffusion coefficient is kept constant; the same is done for the diffusion coefficient D (i.e. k_{off} is adjusted in a way that the effective diffusion coefficient is kept constant). After this procedure, two confidence intervals have been determined for each fit parameter, and the larger one is reported. The independent confidence intervals for the fit parameters, which are calculated in the first step, determine the error of their ratios and are used in order to calculate the confidence intervals for all quantities depending on these ratios, i.e. the effective diffusion coefficient, the pseudo-affinity and the sizes of the free and the bound fraction.

Evaluation of fit quality and comparison of different models. For comparison between different experiments, the fit evaluation must be independent of the number of data points (unlike the sum of residuals χ^2). *FREDIS* calculates the coefficient of determination R^2, which fulfills these requirements.

$$R^2 = \frac{\sum_i \left(frap_i - \overline{frap} \right)^2}{\sum_i \left(frap_i - model_i \right)^2} \qquad (14)$$

The parameter $frap_i$ denotes the value of the measured recovery curve at time-point i, $\overline{frap}$ is the mean of $frap_i$ and $model_i$ the value of the fitted recovery curve. For $R^2 = 1$, the measured and the calculated recovery curve are identical; for $R^2 = 0$, a horizontal line (at the mean of the measured recovery curve) would result in an equally good fit as the fit obtained.
The coefficient R^2 can be used to compare fits of models with the same number of parameters, i.e. to compare different data sets fitted with the same model to each other or to compare a data set fitted with the pure reaction model to a data set fitted with the pure diffusion model. However, if a fit with the reaction-diffusion model has to be compared to one of the simpler models, the different numbers of fit parameters have to be considered, since a fit is expected to be better if more fit parameters can be adjusted. Moreover, the fit with one of the simpler models cannot be better than the fit with the reaction-diffusion model because the simpler models are limiting cases of the reaction-diffusion model and all possible recovery curves calculated with the simpler models can be obtained with the appropriate

parameter set according to the reaction-diffusion model as well. In order to incorporate the different numbers of fit parameters into the analysis, the ratio F is calculated

$$F = \frac{\chi_1^2 - \chi_2^2}{\chi_2^2} \frac{df_2}{df_1 - df_2} = \frac{\chi_1^2 - \chi_2^2}{\chi_2^2} \frac{n - p_2}{p_2 - p_1} \qquad (15)$$

with the sum of residuals for the fit with the i-th model χ_i^2, the degrees of freedom for the i-th model df_i, the number of fit parameters for the i-th model p_i and the number of data points n. The value of F represents the ratio between the relative change in the sum of residuals and the relative change in degrees of freedom for the two models. In the calculation performed by *FREDIS*, the simpler model corresponds to model 1 and the reaction-diffusion model corresponds to model 2. Thus, an F ratio greater than 1 means that the sum of residuals has decreased more than expected (going from the simpler model to the reaction-diffusion model) and the reaction-diffusion model is the better description. If the F ratio is smaller than 1, the opposite is the case and the simpler model is the better description. Based on the F ratio, a P value is determined according to Eq. 16.

$$P = 1 - cdf_f(F, m, n) \qquad (16)$$

The parameter cdf_f represents the cumulative density function for F as defined in Eq. 15, m and n are the degrees of freedom of the nominator and the denominator. The P value tests the null hypothesis that both models fit equally well to the data. It can be interpreted as the probability to obtain a given F ratio (i.e. a given difference in the sum of residuals) by chance. Thus, a low P value indicates a significant difference between the models, a high P value only a slight difference. For every reaction-diffusion fit, *FREDIS* reports the F and P by comparing the reaction-diffusion model to the one of the two simple models that provides the better fit.

To extract the lower boundary for the dissociation rate of class I binding sites, reaction-diffusion fits with fixed values for the dissociation rate were performed and compared to fits according to the effective diffusion model. The fixed value for k_{off} was reduced until the reaction-diffusion model fitted significantly worse than the effective diffusion model (according to the criterion given in Eq. 13). This value was considered to be the lower boundary for the dissociation rate.

Continuous fluorescence photobleaching and fluorescence loss in photobleaching

For the CP experiments the laser beam of the CLSM was parked at the position of interest, and the bleaching process at moderate constant intensity was followed over time by recording the fluorescence emission signal. The dynamic equilibrium of photobleaching, diffusion, and dissociation/association processes of fluorescently labeled molecules to an immobilized structure leads to a characteristic decay of fluorescence as previously described in (7, 11, 12). The biphasic behavior of CP curves depends both on the bleaching of an immobilized or transiently bound fraction and on bleaching of the whole pool of freely mobile molecules. Between both fractions a dynamic exchange can take place. The binding interaction was considered as an equilibrium between a freely diffusing molecule F and an immobile receptor S according to $F + S \leftrightarrows FS$, with the dissociation rate k_{off} and the association rate k_{on}.

$$c_{immo}(\vec{r}, 0) / c_{diff}(\vec{r}, 0) = c_B(\vec{r})\, k_{on} / k_{off} \qquad (17)$$

The concentrations c_{immo} and c_{diff} describe the distribution of unbleached bound and free ligands, respectively, and c_{B} denotes the constant concentration of available binding sites within the equilibrium. The diffusive particles contribute to the fluorescence signal according to

$$F_{\text{diff}}(t) = F_{\text{diff}}(0) \cdot \exp\left(-\left(\alpha + k_{\text{on}}\, c_B\right)\frac{V_{\text{eff}}}{V}\, t\right) \qquad (18)$$

where α is the fluorophore-specific bleaching probability, V_{eff} the effective focal volume and V the sample volume. Especially the initial decay in the time course of the fluorescence signal is primarily influenced by photobleaching the permanently immobilized molecules ($k_{\text{off}} = 0$)

$$F_{\text{immo}}(t) = F_{\text{immo}}(0) \cdot \left(1 + \frac{\alpha t}{2} + \frac{\alpha^2 t^2}{6}\right)^{-1} \qquad (19)$$

as well as the (transiently) bound fractions. Transiently bound HP1 features small dissociation rates, thus the particular case of $k_{\text{off}}/\alpha \leq 1$ holds (12):

$$F_{\text{bound}}(t) = F_{\text{bound}}(0) \cdot \left[\begin{array}{l} \left(\left(1 + \frac{\alpha t}{2} + \frac{\alpha^2 t^2}{6}\right)^{-1} - \frac{12\, k_{\text{off}}/\alpha}{5 + 14\, k_{\text{off}}/\alpha}\left(1 + \frac{3\alpha t}{7}\right)^{-1}\right)\exp\left(k_{\text{off}}\, t\right) \\ + \frac{12\, k_{\text{off}}/\alpha}{5 + 14\, k_{\text{off}}/\alpha}\exp\left(-\left(\alpha + k_{\text{on}}\, c_B\right)\frac{V_{\text{eff}}}{V}\, t\right) \end{array}\right] \qquad (20)$$

Therefore the measured fluorescence signal was fitted to the sum of these terms $F_{\text{immo}}(t) + F_{\text{bound}}(t) + F_{\text{diff}}(t)$. Data fitting was performed using a Levenberg-Marquardt algorithm.

In FLIP experiments the fluorescence loss within heterochromatin and euchromatin regions was monitored at low laser power between repetitive bleach pulses (every 1.35 s, within a circular ROI of 3 µm in diameter at 100 % laser intensity) at distant regions from the bleach spot within the same nucleus. The acquisition of 10 prebleach images was followed by 200 postbleach-images. Data were corrected for background and acquisition photobleaching and were normalized (13). The relative fluorescence was plotted against time and the differences in fluorescence between heterochromatin and euchromatin were calculated.

Fluorescence correlation spectroscopy

Confocal images were taken to determine the regions for the fluctuation measurements in cytoplasm, euchromatin and heterochromatin. Then the concentration fluctuations of fluorescently labeled molecules (around the mean intensity) $\delta F(t) = F(t) - \langle F(t)\rangle$ were recorded for 60 s and the intensity signal was subjected to a time correlation analysis to obtain the autocorrelation function (ACF)

$$G(\tau) = \frac{\langle \delta F(t)\, \delta F(t+\tau)\rangle}{\langle F(t)\rangle^2} \qquad (21)$$

as described previously (7, 14, 15). The data were fitted to an anomalous diffusion model, which is characterized by a nonlinear time dependency of the mean squared particle displacement given by the anomaly parameter α (7, 16-19):

$$\left\langle r^2(t)\right\rangle = 2n\,D(t)\,t \propto t^{\alpha} \qquad (22)$$

Additional parameters for fitting the FCS curve include the intrinsic photophysical dynamics of the fluorescent proteins, like triplet states, whose probability is given by θ and whose relaxation time is τ_T (20), yielding Eq. 23:

$$G(\tau) = \frac{1}{N}\left(1-\theta+\theta\exp\left(-\frac{\tau}{\tau_T}\right)\right)\cdot\left(1+\left(\frac{\tau}{\tau_{\text{diff}}}\right)^{\alpha}\right)^{-1}\left(1+\frac{1}{\kappa^2}\left(\frac{\tau}{\tau_{\text{diff}}}\right)^{\alpha}\right)^{-1/2} \qquad (23)$$

Here N represents the number of particles and $\tau_{\text{diff}} = \omega_0^2/4D$ the mean dwell time inside the focus with a lateral radius ω_0. The structure parameter κ is the ratio of the axial and lateral focus radius. Correlation data were fitted either to a one- or two-component model of anomalous diffusion or to a two-component model, where the first component followed anomalous diffusion and the second component was assumed to be bound to a slowly, confinedly moving lattice. The simplest way to model confined diffusion due to binding is to regard Brownian motion within a harmonic potential (with the friction coefficient γ and the spring constant k) (21). Therefore the second component of the ACF changes to:

$$\begin{aligned} G_{\text{bound}}(\tau) &= \frac{1}{N}\left(1-\theta+\theta\exp\left(-\frac{\tau}{\tau_T}\right)\right) \\ &\cdot\left[\left(1+\frac{1-\exp\left(-k\tau/\gamma\right)}{\eta}\right)^{-1}\left(1+\frac{1-\exp\left(-k\tau/\gamma\right)}{\kappa^2\eta}\right)^{-1/2} - \left(1+\frac{1}{\eta}\right)^{-1}\left(1+\frac{1}{\kappa^2\eta}\right)^{-1/2}\right] \end{aligned} \qquad (24)$$

η is the ratio of τ_{diff}, the dwell time of free diffusion within the focal volume, and the relaxation time $\tau_{\text{relax}} = \gamma/k$. The calculation of the correlation functions was done with the Fluctuation Analyzer software (version 1.1 by M. Wachsmuth). Curve fitting was done with a fixed triplet correction term of τ_T = 100 µs for GFP. From the *in vivo* measurements we obtained the number of molecules N and a diffusion-induced correlation time τ_{diff}. Based on N and τ_{diff} the molecule concentration $c = N/V_{\text{eff}}$ and the apparent diffusion coefficients $D = \omega_0^2/4\tau_{\text{diff}}$ can be calculated.

The calibration of the focal volume dimensions was done with Alexa Fluor 488 C5 maleimide (Invitrogen, Molecular Probes) dissolved in water, which has a diffusion coefficient of $D_{\text{Alexa488}} = (2.1 \pm 0.21)\cdot 10^{-6}$ cm²/s (21). The diffusion coefficient of Alexa Fluor 488 in water was used to measure the device-specific parameter κ and calculate the lateral and axial beam dimension ($\omega_0 = \sqrt{4D_{\text{Alexa}}\tau_{\text{Alexa}}}$ and $z_0 = \kappa\omega_0$) as well as the effective focus volume $V_{\text{eff}} = \pi^{3/2}\omega_0^2 z_0$. The averaged values of ω_0 and z_0 were 0.17 ± 0.01 µm and 0.78 ± 0.06 µm and therefore the observation volume was about 0.13 ± 0.01 fl. At least 10 experiments each for HP1α and for HP1β in the three compartments cytoplasm, euchromatin and heterochromatin were evaluated.

Comparing diffusion coefficients obtained by FCS and FRAP

The effective diffusion coefficient for class I binding determined in heterochromatin by FRAP was $D_{FRAP} = 0.9 \pm 0.5$ µm² s^{-1}, the corresponding value determined by FCS was $D_{FCS} = 3.9 \pm 0.9$ µm² s^{-1}. Since these were determined on different length scales, the diffusion constants were related according to Eq. 25:

$$\frac{D_{FCS}}{D_{FRAP}} = \left(\frac{{w_{FCS}}^2}{{w_{FRAP}}^2} \right)^{(\alpha-1)/\alpha} = \left(\frac{(170\ \text{nm})^2}{(950\ \text{nm})^2} \right)^{(\alpha-1)/\alpha} \qquad (25)$$

Based on the anomaly parameter α that was determined to be 0.81 ± 0.04 in euchromatin and 0.88 ± 0.12 in heterochromatin $D_{FCS}/D_{FRAP} = 2.2$ [1.8 … 2.8] in euchromatin and $D_{FCS}/D_{FRAP} = 1.6$ [1.0 … 3.0] in heterochromatin was calculated from Eq. 25.

References

1. Jegou, T., I. Chung, G. Heuvelmann, M. Wachsmuth, S. M. Görisch, K. Greulich-Bode, P. Boukamp, P. Lichter, and K. Rippe. 2009. Dynamics of telomeres and promyelocytic leukemia nuclear bodies in a telomerase negative human cell line. Mol. Biol. Cell 20:2070-2082.
2. Peters, A. H., D. O'Carroll, H. Scherthan, K. Mechtler, S. Sauer, C. Schofer, K. Weipoltshammer, M. Pagani, M. Lachner, A. Kohlmaier, S. Opravil, M. Doyle, M. Sibilia, and T. Jenuwein. 2001. Loss of the Suv39h histone methyltransferases impairs mammalian heterochromatin and genome stability. Cell 107:323-337.
3. Axelrod, D. 1977. Cell surface heating during fluorescence photobleaching recovery experiments. Biophys J 18:129-131.
4. Simon, J. R., A. Gough, E. Urbanik, F. Wang, F. Lanni, B. R. Ware, and D. L. Taylor. 1988. Analysis of rhodamine and fluorescein-labeled F-actin diffusion in vitro by fluorescence photobleaching recovery. Biophys J 54:801-815.
5. Jain, R. K., R. J. Stock, S. R. Chary, and M. Rueter. 1990. Convection and diffusion measurements using fluorescence recovery after photobleaching and video image analysis: in vitro calibration and assessment. Microvasc Res 39:77-93.
6. Tour, O., R. M. Meijer, D. A. Zacharias, S. R. Adams, and R. Y. Tsien. 2003. Genetically targeted chromophore-assisted light inactivation. Nat Biotechnol 21:1505-1508.
7. Wachsmuth, M., and K. Weisshardt. 2007. Fluorescence Photobleaching and Fluorescence Correlation Spectroscopy: Two Contemplementary Technologies To Study Molecular Dynamics in Living Cells. In Imaging Cellular and Molecular Biological Functions. S. L. Shorte, and F. Frischknecht, editors. Springer Verlag, Berlin, Heidelberg. 183-234.
8. Sprague, B. L., R. L. Pego, D. A. Stavreva, and J. G. McNally. 2004. Analysis of binding reactions by fluorescence recovery after photobleaching. Biophys J 86:3473-3495.
9. Mueller, F., P. Wach, and J. G. McNally. 2008. Evidence for a common mode of transcription factor interaction with chromatin as revealed by improved quantitative fluorescence recovery after photobleaching. Biophys J 94:3323-3339.
10. Seber, G. A. F., and C. J. Wild. 2003. Nonlinear Regression. John Wiley and Sons, New York.
11. Wachsmuth, M., M. Caudron-Herger, and K. Rippe. 2008. Genome organization: Balancing stability and plasticity. Biochim Biophys Acta 1783:2061-2079.
12. Wachsmuth, M., T. Weidemann, G. Muller, U. W. Hoffmann-Rohrer, T. A. Knoch, W. Waldeck, and J. Langowski. 2003. Analyzing intracellular binding and diffusion with continuous fluorescence photobleaching. Biophys. J. 84:3353-3363.
13. Rabut, G., and J. Ellenberg. 2005. Photobleaching Techniques to Study Mobility and Molecular Dynamics of Proteins in Live Cells: FRAP, iFRAP, and FLIP. In Live Cell

Imaging - A laboratory manual. R. D. Goldman, and D.L.Spector, editors. Cold Spring Harbor Laboratory Press, Cold Spring Harbor, New York. 101-126.
14. Schwille, P. 2001. Fluorescence Correlation Spectroscopy and Its Potential for Intracellular Applications. Cell Biochemistry and Biophysics 34:383-408.
15. Haustein, E., and P. Schwille. 2003. Ultrasensitive investigations of biological systems by fluorescence correlation spectroscopy. Methods 29:153-166.
16. Saxton, M. J. 1994. Anomalous diffusion due to obstacles: a Monte Carlo study. Biophys. J. 66:394-401.
17. Schwille, P., J. Korlach, and W. W. Webb. 1999. Fluorescence correlation spectroscopy with single-molecule sensitivity on cell and model membranes. Cytometry 36:176-182.
18. Masuda, A., K. Ushida, and T. Okamoto. 2005. New fluorescence correlation spectroscopy enabling direct observation of spatiotemporal dependence of diffusion constants as an evidence of anomalous transport in extracellular matrices. Biophys J 88:3584-3591.
19. Wachsmuth, M., W. Waldeck, and J. Langowski. 2000. Anomalous diffusion of fluorescent probes inside living cell nuclei investigated by spatially-resolved fluorescence correlation spectroscopy. J Mol Biol 298:677-689.
20. Widengren, J., Ü. Mets, and R. Rigler. 1995. Fluorescence Correlation Spectroscopy of Triplet States in Solution: A Theoretical and Experimental Study. J. Phys. Chem. 99:13368-13379.
21. Wachsmuth, M. 2001. Fluoreszenzfluktuationsmikroskopie: Entwicklung eines Prototyps, Theorie und Messung der Beweglichkeit von Biomolekülen im Zellkern. In Fakultät für Physik und Astronomie. Ruprecht-Karls-Universität Heidelberg, Heidelberg.
22. Humphrey, W., A. Dalke, and K. Schulten. 1996. VMD: visual molecular dynamics. J Mol Graph 14:33-38, 27-38.
23. Ormo, M., A. B. Cubitt, K. Kallio, L. A. Gross, R. Y. Tsien, and S. J. Remington. 1996. Crystal structure of the Aequorea victoria green fluorescent protein [see comments]. Science 273:1392-1395.
24. Pearlman, D. A., D. A. Case, J. W. Caldwell, W. R. Ross, T. E. Cheatham III, S. DeBolt, D. Ferguson, G. Seibel, and P. Kollman. 1995. AMBER, a computer program for applying molecular mechanics, normal mode analysis, molecular dynamics and free energy calculations to elucidate the structures and energies of molecules. Comp. Phys. Commun. 91:1-41.
25. Case, D. A., T. A. Darden, T. E. I. Cheatham, C. L. Simmerling, J. Wang, R. E. Duke, R. Luo, K. M. Merz, D. A. Pearlman, M. Crowley, R. Walker, W. Zhang, B. Wang, S. Hayik, A. Roitberg, G. Seabra, K. F. Wong, F. Paesani, X. Wu, S. Brozell, V. Tsui, H. Gohlke, L. Yang, C. Tan, J. Mongan, V. Hornak, G. Cui, P. Beroza, D. H. Mathews, C. Schafmeister, W. S. Ross, and P. A. Kollman. 2006. Amber 9. University of California, San Francisco.
26. Garcia De La Torre, J., M. L. Huertas, and B. Carrasco. 2000. Calculation of hydrodynamic properties of globular proteins from their atomic-level structure. Biophys. J. 78:719-730.

Supplementary Tables

Table S1. Hydrodynamic calculations for HP1 and GFP-tagged HP1.

	GFP	HP1	$(HP1)_2$	GFP-HP1	GFP-HP1·HP1	$(GFP-HP1)_2$
M (kDa)	25.6	21.4	42.8	48.5	71.3	99.8
$\bar{V}$ (kDa)	0.736	0.726	0.726	0.729	0.73	0.73
f ($\mu m^2\ s^{-1}$)	$4.8 \cdot 10^{-11}$	$6.1 \cdot 10^{-11}$	$7.5 \cdot 10^{-11}$	$6.6 \cdot 10^{-11}$	$7.6 \cdot 10^{-11}$	$8.5 \cdot 10^{-11}$
D_{H2O} ($\mu m^2\ s^{-1}$)	103.0	76.1	61.2	69.8	61.4	54.6
D_{cell} ($\mu m^2\ s^{-1}$)	33.1	24.4	19.6	22.3	19.6	17.5

From a model structure of HP1 the basic hydrodynamic properties were calculated and the diffusion coefficients of GFP, HP1, and HP1 constructs in water were derived. M is the molecular weight, $\bar{v}$ is the partial specific volume, f is the friction coefficient and D is the diffusion coefficient at 25 °C. The value of D_{cell} includes an apparent 3.5 times higher intracellular viscosity than that of pure water (as determined for GFP). The molecular visualization program VMD (visual molecular dynamics, www.ks.uiuc.edu/Research/vmd, (22)) was used to build structures of mouse HP1β dimers fused to GFP by employing the corresponding crystal structures (23). The 14 amino acid linker between HP1 and GFP was modeled as a random coil. The energy-minimizing procedure and short molecular dynamics simulations were carried out with Amber 9 (http://ambermd.org/, (24, 25)). Hydrodynamic parameters were calculated with the program HYDROPRO with a sphere radius of 3.1 Å (version 7c, 2005; (26)). Molecular weight and the partial specific volume $\bar{v}$ were calculated using the program Sednterp (Sedimentation interpretation program, version 1.09, Hayes D.B. et al, University of New Hampshire, 1995).

Table S2. Concentrations of endogenous HP1α and GFP-HP1α in NIH 3T3 cells.

	Cytoplasm (µmol liter^{-1})	Euchromatin (µmol liter^{-1})	Heterochromatin [a] (µmol liter^{-1})
GFP-HP1α [b]	0.16 ± 0.11	0.87 ± 0.07	2.1 ± 0.3
HP1α (one allele) [b]	0.04 ± 0.03	0.21 ± 0.03	0.5 ± 0.1
endogenous HP1α [c]	0.08 ± 0.05	0.41 ± 0.05	1.0 ± 0.2

The concentration of GFP-HP1α was determined by FCS measurements as the number of particles within the effective focus volume. Thus, in the table the particle concentrations are listed and the total concentration of monomeric HP1α units will depend on its association state in the cell. In the cytoplasm the diffusion coefficients determined by FCS indicate the presence of HP1α monomers, while the higher concentrations in the nucleus could promote the dimerization of HP1α.

[a] The HP1 concentration in heterochromatin were corrected for the 10 % immobile fraction within heterochromatin, which was bleached during FCS measurements.

[b] Concentrations refer to the 3T3-HP1α cell line that stably expresses GFP-HP1α. Endogenous HP1α concentrations in this cell line were determined from the ratio of GFP-HP1α to HP1α measured on quantitative Western blots (Fig. S3 B) and represent the expression level of HP1α from one allele.

[c] HP1α concentrations were calculated for two alleles, corresponding to the HP1α concentration in NIH 3T3 reference cells.

Supplementary Figures

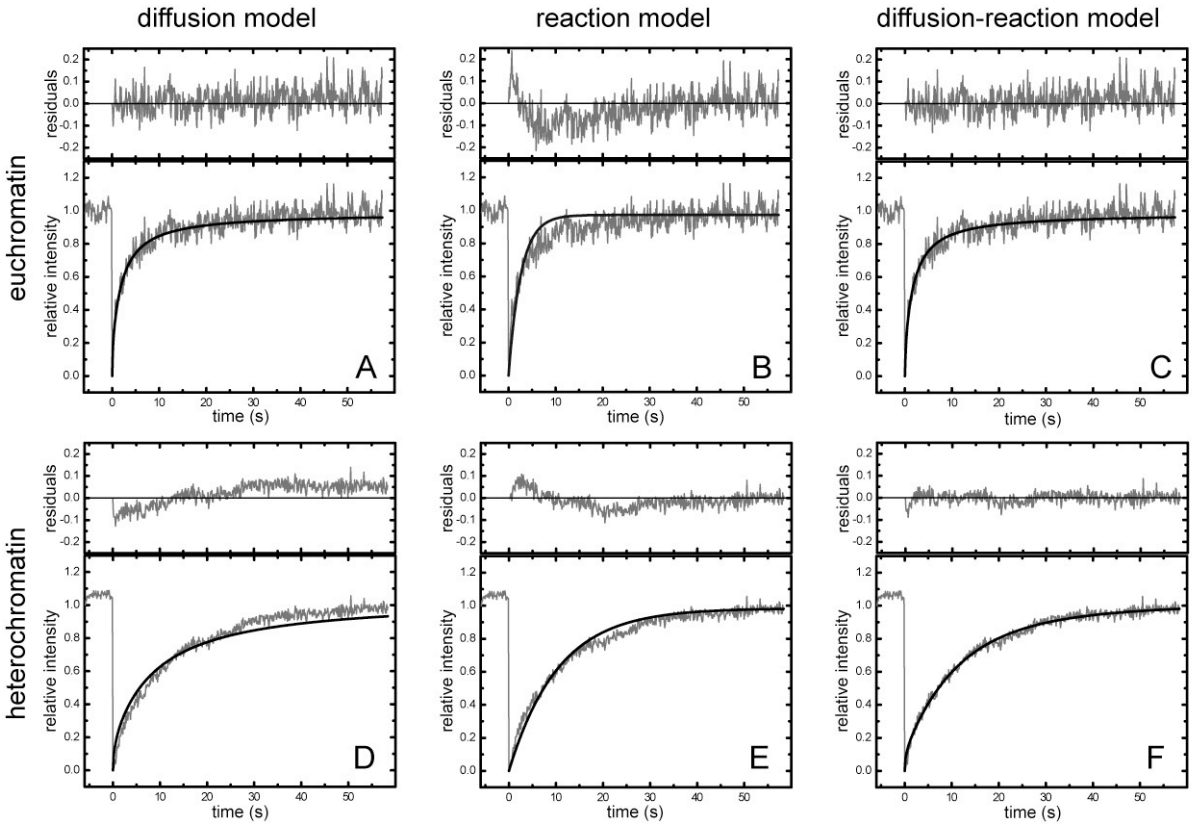

Figure S1. Kinetic modeling of the FRAP data recorded for HP1α in the 3T3-HP1α cell line in euchromatin (A-C) and heterochromatin (D-F). As described above three different mathematical models were used for curve fitting, a diffusion-dominant model (A, D; Eq. 10), a reaction-dominant model (B, E; Eq. 11) and a diffusion-reaction model that combines both reaction processes (C, F; Eq. 11). Above the graphs the residuals of the fits are shown. While for euchromatin a pure diffusion model resulted in a good fit, the description of HP1α mobility in heterochromatin required the use of the diffusion-reaction model for a good fit to the data. This was confirmed in a statistical test, in which an average value of $F = 94$ according to Eq. 15 was obtained in a comparison with the simpler models.

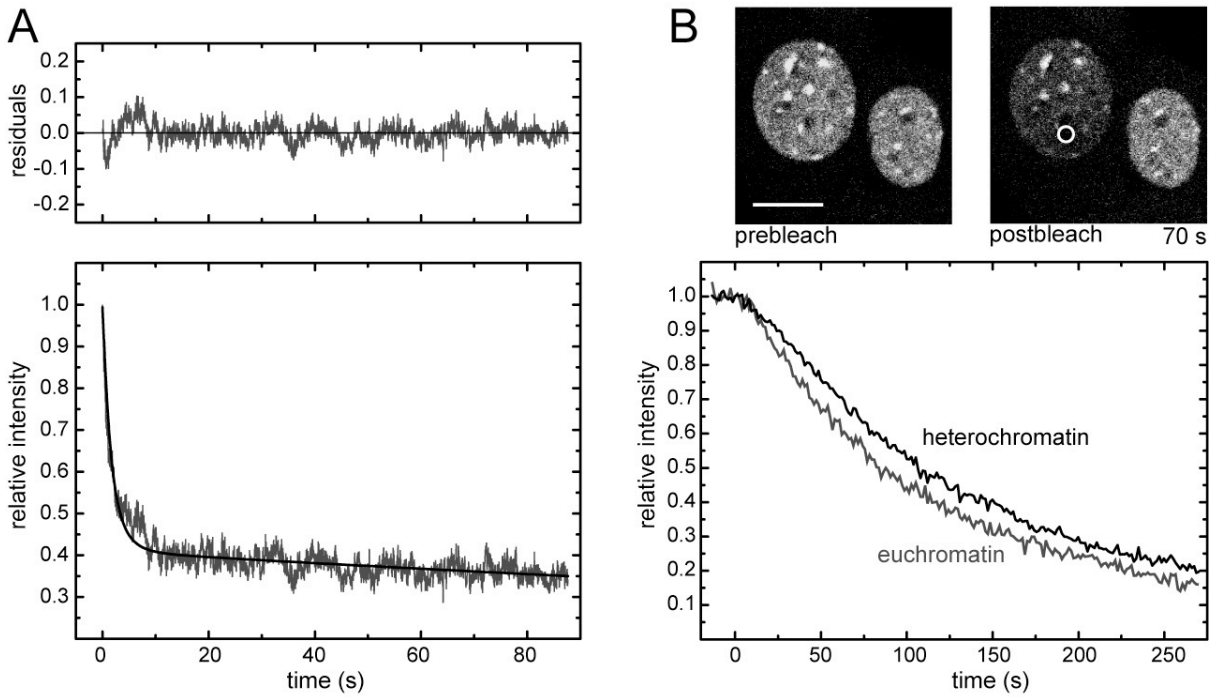

Figure S2. Continuous fluorescence photobleaching and fluorescence loss in photobleaching experiments. (**A**) The initial fast decay of the curve in the continuous photobleaching experiments corresponds to the bleaching of bound GFP-HP1 molecules. From the subsequent continuous exchange of molecules the kinetic dissociation rate k_{off} is determined as described in the text. (**B**) Averaged FLIP curves of heterochromatin versus euchromatin loci within the same cell are depicted. The difference reveals the stably bound 10 % fraction of GFP-HP1α only present in heterochromatin.

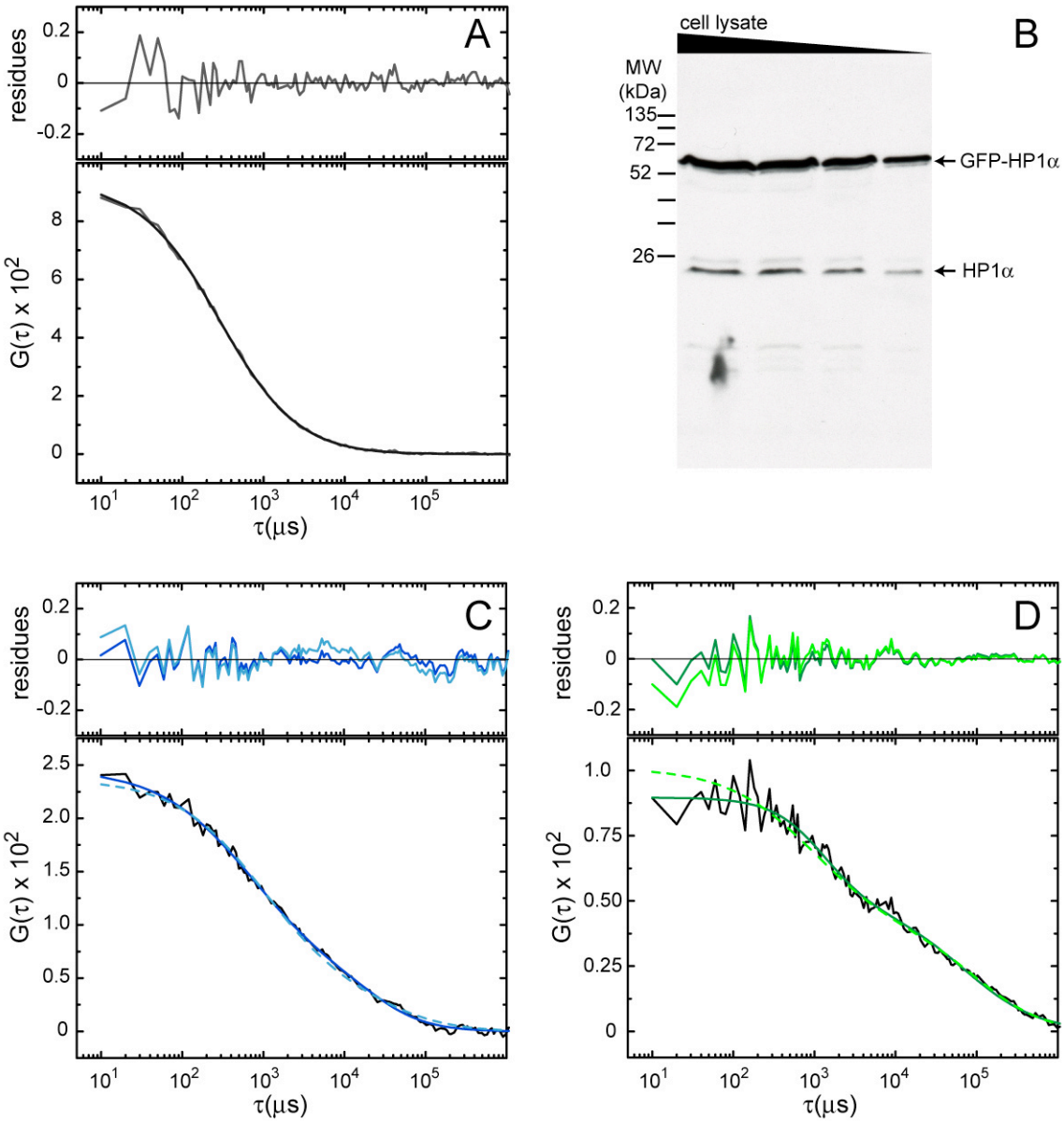

Figure S3. Analysis of HP1α in different cellular compartments by FCS. (**A**) ACF of HP1α in the cytoplasm fitted with an anomalous diffusion model. HP1α concentrations were determined by FCS experiments as the number of particles within the effective focus volume as described above and in Table S2. (**B**) The concentration of endogenous HP1α was determined from the ratio of GFP-tagged HP1α to untagged HP1α in the stable GFP-HP1α cell line by quantitative Western blots with an HP1α antibody. The two bands corresponding to GFP-HP1α and endogenous HP1α can be clearly identified. The concentration of endogenous HP1α can be determined by the relative ratio of the two signals on the western blot and the FCS concentration measurement of GFP-HP1α. (**C**) Representative ACF in euchromatin. The second fraction is likely to represent HP1α bound to slowly moving chromatin. Accordingly, the data were also fitted to a confined diffusion model (dashed curves), leading to an equally good fit as the anomalous diffusion description (solid line). (**D**) Same as in panel C but for heterochromatin.